UKAEA-CCFE-PR(21)84

Daniel R. Mason, Abdallah Reza, Fredric Granberg,
Felix Hofmann

An estimate for thermal diffusivity in highly irradiated tungsten using Molecular Dynamics simulation

Enquiries about copyright and reproduction should in the first instance be addressed to the UKAEA Publications Officer, Culham Science Centre, Building K1/0/83 Abingdon, Oxfordshire, OX14 3DB, UK. The United Kingdom Atomic Energy Authority is the copyright holder.

The contents of this document and all other UKAEA Preprints, Reports and Conference Papers are available to view online free at scientific-publications.ukaea.uk/

An estimate for thermal diffusivity in highly irradiated tungsten using Molecular Dynamics simulation

Daniel R. Mason, Abdallah Reza, Fredric Granberg, Felix Hofmann

This is a preprint of a paper submitted for publication in
Physical Review Materials

An estimate for thermal diffusivity in highly irradiated tungsten using Molecular Dynamics simulation

Daniel R. Mason,[1] Abdallah Reza,[2] Fredric Granberg,[3] and Felix Hofmann[2]
[1] *UK Atomic Energy Authority, Culham Science Centre, Oxfordshire OX14 3DB, UK*[*]
[2] *Department of Engineering Science, University of Oxford, Parks Road, OX1 3PJ, UK*[†]
[3] *Department of Physics, University of Helsinki, P.O. Box 43, FI-00014, Helsinki, Finland*

(Dated: May 2021)

The changing thermal conductivity of an irradiated material is among the principal design considerations for any nuclear reactor, but at present few models are capable of predicting these changes starting from an arbitrary atomistic model. Here we present a simple model for computing the thermal diffusivity of tungsten, based on the conductivity of the perfect crystal and resistivity per Frenkel pair, and dividing a simulation into perfect and athermal regions statistically. This is applied to highly irradiated microstructures simulated with Molecular Dynamics. A comparison to experiment shows we closely track observed thermal diffusivity over a range of doses from the dilute limit of a few Frenkel pairs to the high dose saturation limit at 3 displacements per atom (dpa).

INTRODUCTION

Tungsten has been chosen as a plasma facing material designs for future tokamak fusion reactors [1–3] due to its low sputtering yield, high melting point and high thermal conductivity [4]. But under bombardment from 14.1 MeV fusion neutrons, displacement damage within the bulk material will generate lattice defects [5] which can adversely affect thermal conductivity among other properties [6].

Unfortunately, predicting thermal conductivity based on the damage microstructure is extremely difficult, as metal conductivity is dominated by electrons, and so requires a quantum mechanical treatment. The electron scattering rate can be written down from Fermi's golden rule as proportional to the square of a perturbing matrix element coupling two electron states. For the electron-phonon coupling this can be computed from the elastic deformation due to the phonon [7]. In semiconductors at least sufficient electron localisation is present to permit fast scaling methods using Density Functional Perturbation Theory [8]. In metals these calculations are expensive and while transport calculations can be performed in the Boltzmann theory approximation [9], and scattering rates can be found [10–12], current state-of-the-art ground-state density functional calculations of dislocation loops are limited to order one thousand atoms [13]. When this scale is compared to the minimum size for generating high dose microstructures, order one million atoms [14], we must concede that electronic structure calculations must be supplemented by more approximate methods if a fully multiscale picture of a material's response to stress, temperature and irradiation is to be developed.

This simplifying approach was followed by Zinkle (ref [15]), who suggested a model for the resistivity of circular dislocation loops in copper based on counting defected atoms observed in TEM images and dividing these into dislocation core sites and atoms in stacking fault sites. Reza et al. [16] considered similar models, again based on TEM observations of atoms. It is noteworthy that both these papers required an extrapolation of the distribution of observed loops to sizes too small to observe [17, 18]. Caturla et al. [19] modelled resistivity changes during post irradiation annealing using the resistivity per Frenkel pair, following the count of pairs using kinetic Monte Carlo.

We argue that to predict a thermal conductivity for engineering purposes it is sufficient to be able to divide an arbitrarily complex, atomically-detailed simulated microstructure into regions which are essentially perfect crystal, regions which are elastically distorted and so are somewhat more scattering, and regions which are highly distorted and have substantially greater scattering. If we can robustly predict and characterize an irradiated material along these lines, and reproduce the scattering rate of a simple defect types, we should be able to reproduce the trends in conductivity change due to irradiation dose, temperature, stress and other external drivers through their effect on the microstructure, even if the scattering rate for an individual complex defect type is not exactly reproduced.

Existing methods for distinguishing athermal atoms from bulk crystal atoms include analysing bond angle distributions, common neighbour analysis and graphs of connected bonds [20, 21]. Progress has also been made recently to detect athermal atoms based on Machine Learning [22]. We distinguish perfect lattice from distorted using local potential energy- a property generally available using empirical potentials even if not well-defined in an ab-initio calculation. This choice is made because we can derive an expression for the expected *distribution* of atomic potential energy for a system in thermal equilibrium, combining the Maxwell-Boltzmann distribution with the Debye-Waller factors for thermal vibrations. We demonstrate that this distribution is a very good fit to MD simulations.

We then use a simple model for the scattering rate based on Mattheisen's rule [23] for summing rate contributions on an atom-by-atom basis. We use an empirical model for the scattering rate due to an atom in a defected configuration [24]. With this model, we can uniquely define the thermal conductivity of arbitrarily complex atomic configurations without any parameterization beyond the scattering rate per Frenkel pair. We then describe how to parameterize an empirical potential to fit thermal conductivity quantities which have been experimentally determined for many metallic elements.

Finally we describe how high dose microstructures have been generated at an atomistic level, and how the thermal diffusivity of comparable high-dose tungsten was measured experimentally. We discuss our results from the simulations and compare to the experiment.

THEORY

We can write a simple kinetic theory expression for the electronic thermal conductivity,

$$\kappa = \frac{1}{3\Omega_0} c_e v_F^2 \langle r_e \rangle^{-1}, \tag{1}$$

where c_e is the electronic heat capacity per atom,Ω_0 is the atomic volume, v_F is the Fermi velocity, and r_e is the electron scattering rate. The heat capacity is given in terms of the temperature T and density of states at the Fermi level D_F, $c_e = (\pi^2 k_B^2 D_F/3)T$. Electron scattering comprises contributions from impurity scattering, electron-phonon scattering and electron-electron scattering, with the condition that the mean free path cannot drop below the nearest neighbour separation b_0 [24].

$$\frac{1}{r_e} = \frac{b_0}{v_F} + \frac{1}{r_{imp} + r_{e-ph} + r_{e-e}}. \tag{2}$$

We expect impurity scattering to arise from electrons scattering from the anomalous electrostatic potential at defected sites, impurity atoms and the like, and so be temperature independent. Electron-phonon scattering should be proportional to the number of phonons, and so scale linearly with T. Finally electron-electron scattering should scale with T^2. It is beyond the scope of this work to derive expressions for the latter two terms, so instead we fit to the known variation of thermal conductivity with temperature, and write $r_{e-ph} = \sigma_1 T$, and $r_{e-e} = \sigma_2 T^2$ [25]. We note that this implies our model has an unphysical infinite conductivity for the perfect lattice at zero temperature; in reality there will always be some residual defects and scattering between s- and d- bands in transition metals [26], but resistivity ratios $\rho(273\text{K})/\rho(4.2\text{K})$ of order 10^5 can be measured for very pure single crystal tungsten samples [27].

In this work we focus on the impurity scattering. The experimental literature for scattering rates for specific defects is sparse, owing to the difficulty of knowing exactly which defects are present, but we summarise some important results. In ref [28], the electrical resistivity per vacancy in tungsten was observed to be proportional to linear strain. Secondly, if the resistivity per Frenkel pair [29] is compared to the resistivity per vacancy [30] for molybdenum and tungsten, we find similar ratios of 3.1 and 3.9 respectively. Thirdly, in ref [10], the resistivity for point defect pairs in copper (divacancy and di-interstitial) is calculated to be slightly under double the single point defect value, consistent with best estimates from experiment. These three results suggest that the defect scattering rate must correlate with excess energy: the formation energy per vacancy is expected to vary linearly with strain, with the (tensorial) coefficient being the dipole tensor [31]. The formation energy ratios of Frenkel pair to vacancy computed by DFT (using AM05 potential) for Mo and W are 3.5 and 4.0 respectively [32], which is a reasonable fit to the second observation. The third observation would be consistent with a small binding energy for point defects. We therefore suggest an empirical model, $r_{e-ph} = \sigma_0 |E|$, where E is the excess potential energy of a defected atom [24, 33]. Note that we use the modulus to prevent unphysical negative rates; in practice few defected atoms have negative excess energies, so for the purposes of exposition it is convenient to assume scattering rate from a defect at low temperature is proportional to its formation energy. How we define excess energy, and whether an atom is defected or not is given below.

Consider a system of atoms thermalized using classical molecular dynamics at temperature T with an empirical many body potential. The population of a phonon mode energy $E = \hbar\omega$ is given by the Boltzmann distribution, $p_B(E;T)dE = 2\beta \exp[-2\beta E]dE$, where $\beta = 1/k_B T$ is the inverse temperature. From this, it is straightforward to show that the kinetic energy of each atom follows the Maxwell-Boltzmann distribution, $p_{M-B}(E;T)dE = \beta(2\beta E)^2 \exp[-2\beta E]dE$. The potential energy of each atom does not quite follow this distribution, as the atoms are not Einstein oscillators but rather have local energies determined by the distances to their neighbours. But if we assume that for thermally equilibrated atoms, they nevertheless appear to be close to Einstein oscillators, we can say the probability distribution of the position of each atom is in turn close to a spherically symmetric Gaussian. This approximation is often used in constructing Debye-Waller factors for dynamical electron diffraction calculations: the Debye-Waller factor, B, is related to the thermally averaged atom displacement in the $x-$ direction, $B = 8\pi^2 \langle u_x^2 \rangle$, where in the harmonic approximation [34],

$$\langle u_x^2 \rangle = \left(\frac{\hbar}{2m}\right) \int \coth\left(\frac{\hbar\omega}{2k_B T}\right) \frac{g(\omega)}{\omega} \mathrm{d}\omega, \tag{3}$$

with $g(\omega)$ being the normalised phonon density of states.

We can find the temperature scaling of this displacement scale by using the Debye formula in place of the density of states, to give[35]

$$\langle u_x^2\rangle = \left(\frac{11492}{8\pi^2 M}\right)\left(\frac{T}{\Theta_D^2}\right)\left(\Phi\left(\frac{\Theta_D}{T}\right)+\frac{1}{4}\left(\frac{\Theta_D}{T}\right)\right), \tag{4}$$

where Θ_D is the Debye temperature and $\Phi(\Theta_D/T)$ is the Debye integral. If M is the atomic mass in Daltons, then $\langle u_x^2\rangle$ is returned in units of $\mathring{A}^2$. Above the Debye temperature (or in classical molecular dynamics where quantum mechanical phonons are not represented), $\langle u_x^2\rangle$ scales linearly with T, and so

$$\langle u_x^2\rangle \sim \frac{145.55}{M\Theta_D^2}T. \tag{5}$$

With this approximation, the probability distribution for the distance between the atoms is *also* Gaussian, albeit with a slightly larger distribution half-width w. If the perfect lattice distance between atoms is $R^{(0)} \gg w$, then the probability distribution at finite temperature is

$$p(R) \approx \frac{1}{\sqrt{2\pi w^2}}\exp\left(-\frac{(R-R^{(0)})^2}{2w^2}\right), \tag{6}$$

with $w^2 = 16\langle u_x^2\rangle/\pi^2 = 2B/\pi^4$. Hence we can say that the standard deviation of the bond-length fluctuations scales as $\sim\sqrt{T}$.

If we assume the thermal vibrations are small, then we can linearise the energy dependence in terms of atomic separations, and so find the probability distribution for potential energies will be approximately given by the convolution of the Maxwell-Boltzmann distribution and a third Gaussian function, $g(E;\sigma) = \exp[-E^2/(2\sigma^2)]/\sqrt{2\pi\sigma^2}$. The preceding arguments suggest that $\sigma^2 \sim \Delta k_B T$, with Δ a potential dependent constant with energy units. It is not an advantage to derive a formula for Δ, as individual empirical potentials will have slightly different Debye temperatures, and we shall see below this parameter is easily found from simulation. With the convolution applied, we find our form for the distribution of potential energies in a thermalised MD simulation:

$$\begin{aligned} p_{\mathrm{MD}}(E;T) &= p_{M-B}(E;T)\otimes g(E;\sigma) \\ &= 2\beta^3\left\{\exp\left[-\frac{E^2}{2\sigma^2}\right]\sqrt{\frac{2\sigma^2}{\pi}}(E-2\beta\sigma^2)\right. \\ &\quad + \exp\left[2\beta^2\sigma^2-2\beta E\right]\left(\sigma^2+(E-2\beta\sigma^2)^2\right) \\ &\quad \left.\times(1+\mathrm{erf}\left(\frac{E-2\beta\sigma^2}{\sqrt{2\sigma^2}}\right)\right\} \end{aligned} \tag{7}$$

The zero of energy is taken here to be the energy per atom at zero temperature with appropriate supercell strains applied, and so E is the excess potential energy.

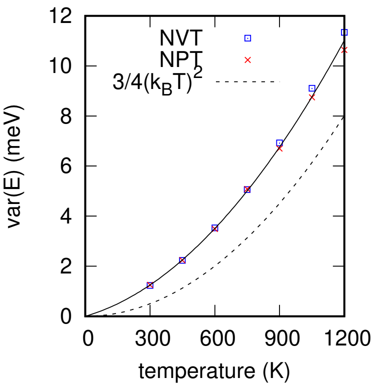

FIG. 1. The variance of the potential energy of 65k atoms thermalized in the NVT and NPT ensembles. The dashed line shows the variance in the Maxwell-Boltzmann distribution, and the solid line is the model including broadening (equation 7) with $\sigma = \sqrt{\Delta(k_B T)}$, with $\Delta = 0.029$ eV.

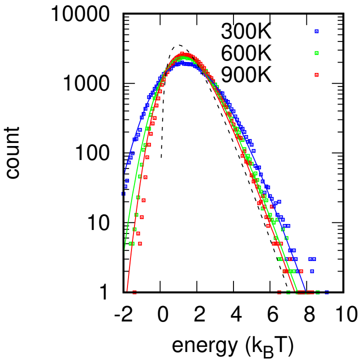

FIG. 2. A histogram of potential energies of 65k atoms thermalized in the NPT ensemble using LAMMPS. The dashed line is the M-B distribution, and the solid lines are a convolution with a Gaussian width $\sigma = \sqrt{\Delta(k_B T)}$ (equation 7).

The first few moments of $p_{MD}(E;T)$ are: $\int p_{\mathrm{MD}}(E;T)dE = 1$, $\int E p_{\mathrm{MD}}(E;T)dE = 3/2k_BT$, and $\int E^2 p_{\mathrm{MD}}(E;T)dE = 3(k_BT)^2+\sigma^2$. The simple form for the second moment means we can parameterize for σ by plotting the variance of the potential energy as a function of temperature. We thermalize a simulation box of 65336 tungsten atoms using LAMMPS [36] and an empirical potential [37] known to give reasonable point defect and thermal expansion properties in the NPT ensemble (constant atom Number, Pressure and Temperature). Figure 1 shows the fit of the variance to $\mathrm{var}(E) = 3/4(k_BT)^2 + \Delta k_BT$ with $\Delta = 0.029 \pm 0.001$ eV. The high quality of a broadened Maxwell-Boltzmann distribution is further shown in figure 2. Here we have generated a histogram of the potential energy per atom for the 65336 atom box in the NPT ensemble. Note that the fit is good even in the tails of the distribution.

If we generate a histogram of potential energies similar to figure 2 but in a defected system of atoms, and compare to the expected thermal distribution (equation 7), we can estimate how many atoms are thermal, and how many are athermal. Note that we can not say for certain whether an individual atom is defected, only find the fraction of athermal atoms in each energy bin.

If there are N atoms total in the system, then we expect to find a number $\bar{N}$ in the energy range $E : E + \mathrm{d}E$ given by $\bar{N}(E;T) = N\, p_{\mathrm{MD}}(E;T)\mathrm{d}E$. The actual number of thermal atoms we record should follow a Poisson distribution with this average, ie the distribution $\Pi(n;\bar{N}) = \bar{N}^n \exp[-\bar{N}]/n!$. If we actually record n atoms in the energy interval, then the probability that k of these are non-thermal atoms must be given by the Poisson probability that $n-k$ are thermal

$$p(k;n,\bar{N}) = \frac{\Pi(n-k;\bar{N})}{\sum_{k=0}^{n} \Pi(n-k;\bar{N})}. \tag{8}$$

The expected number of non-thermal atoms in this energy window is therefore

$$\langle k \rangle = \sum_{k=0}^{n} k\, p(k;n,\bar{N}). \tag{9}$$

Histograms of athermal atom count using equation 9 for systems containing a single point defect are shown in figure 3. Note that the expected number of non-thermal atoms defined in this way tracks the thermal count, simply because this is a stochastic property of the system. (The athermal proportion is order 2% for this potential and system size, a value largely independent of temperature). The true signal of the point defects appears where we expect to see very few thermal atoms. For the monovacancy at 300K, we see a signal at 0.3eV. This is generated by the cage of high energy atoms surrounding the vacancy itself. For the crowdion we see the individual atoms making up this extended defect with very high energy (> 0.5 eV).

We can compute expected scattering rates for thermal atoms using equation 2:

$$r_\theta(T) = \frac{v_F(\sigma_1 T + \sigma_2 T^2)}{b_0(\sigma_1 T + \sigma_2 T^2) + v_F}, \tag{10}$$

and for athermal atoms with

$$r_i(E;T) = \frac{v_F(\sigma_0|E| + \sigma_1 T + \sigma_2 T^2)}{b_0(\sigma_0|E| + \sigma_1 T + \sigma_2 T^2) + v_F}. \tag{11}$$

We can therefore find the expected scattering rate due to electron-phonon and impurity scattering from atoms in the energy window $E : E + dE$ is

$$r(E;T) = \sum_{k=0}^{n} p(k;n,\bar{N}(E;T))\,\left((n-k)r_\theta(T) + k r_i(E;T)\right). \tag{12}$$

and the total scattering rate is

$$r_e = \int r(E;T)dE. \tag{13}$$

In practice we need to generate a histogram, so this integral is computed numerically. The scattering rate is not biased by bin width provided the width is small compared with the temperature scale. We use bin widths $\mathrm{d}E \sim k_B T/20$.

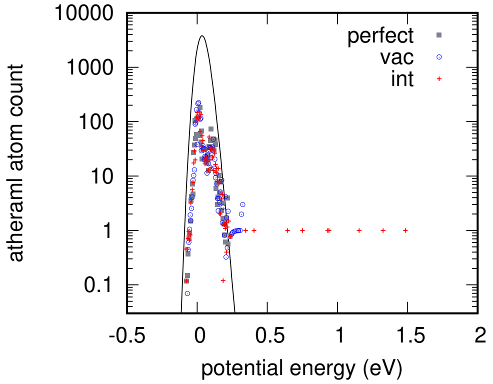

FIG. 3. A histogram of athermal atoms in a system of 65k atoms thermalized in the NPT ensemble at 300K. The solid line shows the expected count of thermal atoms in each bin. The symbols show the predicted number of athermal atoms (equation 9, for a defect-free lattice, and for monovacancy crowdion configurations.

Fitting the model to experiment

In the limit $T \to 0$, all atoms in a perfect crystal have $E = 0$. For a crystal containing a point defect relaxed using conjugate gradients no atoms will have exactly $E = 0$, although most will be in a narrow bin $-\mathrm{d}E/2 : +\mathrm{d}E/2$. Atoms outside this bin can be assumed 'athermal' in the low temperature limit.

Therefore we can compute scattering rate for a defect relaxed using conjugate gradients, assuming a small temperature T were applied to avoid the singularity in the rate at $T = 0$, provided we make some choice for the triplet $\{\sigma_0, \sigma_1, \sigma_2\}$. The scattering rate for a Frenkel pair, $r_{\mathrm{FP}}(T)$, is just the sum of the rates for monovacancy and crowdion. We can then use the Weidemann-Franz law relating electrical resistivity to thermal conductivity, $\rho = LT/\kappa$, where $L = 2.44 \times 10^{-8}$ WΩK^{-2} is the Lorenz number, to match the measured resistivity per Frenkel pair, ρ_{FP} by substituting equation 1:

$$\rho_{\mathrm{FP}} = \lim_{T\to 0} \frac{3L\Omega_0}{v_F^2\,(c_e/T)} r_{\mathrm{FP}}(T). \tag{14}$$

As $\lim_{T\to 0} r_{\mathrm{FP}}(T)$ is linear in σ_0, we can use this to fit σ_0. Using $v_F = 9.5$Å/fs and $c_e/T/\Omega_0 = 5.46 \times 10^{-10}$ eV/K^2/Å^3 computed using Density Functional Theory [24], and the experimental value $\rho_{\mathrm{FP}} = 27$ $\mu\Omega$ m/at.fr. [29], we find a target value $r_{\mathrm{FP}}(T = 0) = 29.1$ fs. Figure 4 shows the fitting of our model to this computed scattering rate per Frenkel pair, achieved by set-

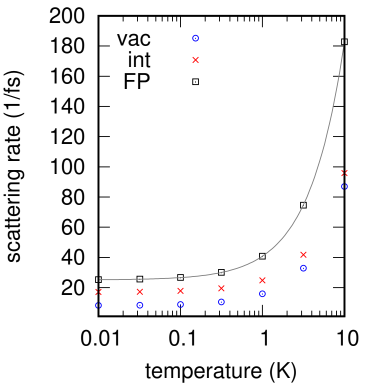

FIG. 4. Scattering rate computed for monovacancy and crowdion point defects in perfect lattice, with assumed temperatures applied. The solid line is an affine fit, so the y-axis intercept gives the scattering rate for the Frenkel pair at $T = 0$.

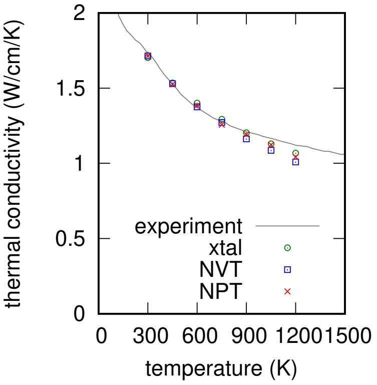

FIG. 5. Thermal conductivity of atoms in a defect-free condition thermalized in the NPT and NVT ensembles, and for the perfect crystal lattice with an assumed temperature. Solid line experimental data from ref[38]

ting $\sigma_0 = 2.32$ fs^{-1}/eV. The error in this value due to the non-linearity of the computed rates $r_{\rm FP}(T)$ is very much smaller than the uncertainty in $\rho_{\rm FP}$.

With σ_0 fixed by the Frenkel pair calculation, we can fit σ_1 and σ_2 to reproduce the experimental thermal conductivity [38]. Many methods to fit the curves would be appropriate here. We performed the fit efficiently by observing (empirically) that the fraction of athermal atoms is very weakly dependent on temperature, in these simulations $f(T) \approx 0.022 + 0.156 k_B T$, and their average energy is linear in temperature, $\langle E \rangle \approx 2.04 k_B T$. With these approximations we write down the expected scattering rate at temperature T as

$$\langle r(T) \rangle \approx f(T) r_i(\langle E \rangle; T) + (1 - f(T)) r_\theta(T),$$

and hence the expected thermal conductivity is

$$\langle \kappa(T) \rangle \approx \frac{c_e v_F^2}{3\Omega_0 \langle r(T) \rangle}. \tag{15}$$

This is then a simple analytic form to fit for $\{\sigma_1, \sigma_2\}$. The thermal conductivity predicted for a defect-free, but MD thermalized lattice at finite temperature is shown in figure 5. We find a fit $\sigma_1^{(MD)} = 1.102 \times 10^{-4}$ fs^{-1}/K and $\sigma_2^{(MD)} = 1.215 \times 10^{-7}$ fs^{-1}/K^2. The points in figure 5 for thermalized systems in the NVT and NPT ensembles use this set of parameters.

We can also fit equation 15 to the experimental data if the atoms are in ideal lattice positions. In this case the only difference is that we would expect no athermal atoms, ie a fraction $f = 0$. This gives a fit which is suited to an atomic system which has been relaxed using conjugate gradients and has no thermal noise. We find $\sigma_1^{(CG)} = 1.191 \times 10^{-4}$ fs^{-1}/K and $\sigma_2^{(CG)} = 1.253 \times 10^{-7}$ fs^{-1}/K^2. The points in figure 5 labelled as perfect crystal use this second set of parameters. Note that $\sigma_1^{(MD)}$ is slightly smaller than $\sigma_1^{(CG)}$ as our statistical model always estimates a small number of atoms in MD are 'athermal' and so are given a higher scattering rate.

Note that in our model we ignore the contribution to thermal conductivity from phonons, which is computable using MD if needed, but here is small compared to electron conductivity. Thermal diffusivity, α, is defined from thermal conductivity as $\alpha = \kappa/c$, where c is the volumetric heat capacity, here dominated by phonons, so $c = 3k_B/\Omega_0$. A summary of the values used to parameterize and resultant conductivity is given for reference in table I.

Fitted parameters

impurity scattering	σ_0	0.232 PHz/eV
el-ph scattering	$\sigma_1^{(MD)}$	1.102×10^{-4} PHz/K
	$\sigma_1^{(CG)}$	1.191×10^{-4}
el-el scattering	$\sigma_2^{(MD)}$	1.215×10^{-7} PHz/K^2
	$\sigma_2^{(CG)}$	1.253×10^{-7}
conductivity const	$\frac{c_e v_F^2}{3\Omega_0 T}$	1.643×10^{-8} eV/K^2/Å/fs^2

Derived properties

energy broadening	Δ	0.029 eV
atomic volume (T=0K)	Ω_0	15.86 (15.86)$^{(a)}$ Å^3
conductivity	κ(T=273K)	1.74 (1.77)$^{(b)}$ W/cm/K
	κ(T=900K)	1.20 (1.21)$^{(b)}$
resistivity	$\rho_{\rm FP}$	27.0 (27)$^{(c)}$ $\mu\Omega$ m/at.fr.
	$\rho_{\rm vac}$	8.11 (7)$^{(d)}$

TABLE I. Parameters fitted to the experimental thermal conductivity as a function of temperature and scattering due to a Frenkel pair in tungsten. Note that the σ parameters are electronic scattering effects which must be added for this work, and are not fitted to the TGS experiments described here. Note we provide values for MD-simulated data and CG-relaxed data. Experimental properties given in parentheses: a) ref [39], b) ref [38], d) ref [30], c) ref [29].

HIGH DOSE MICROSTRUCTURES

MD simulation

To generate some representative simulated microstructures for this study, we employed a two-step process, described in detail in ref [40]. First we used the Creation-Relaxation Algorithm (CRA) [14], which generates high dose microstructures rapidly, but leaves an excessive number of high energy defects, then we relaxed further with low energy molecular dynamics (MD) cascade simulations [41–44].

We start with a box of $64 \times 64 \times 200$ conventional bcc unit cells with a lattice parameter $a_0 = 3.1652 \mathring{A}$. The CRA algorithm then selects some atoms at random, and removes them, leaving vacant sites. These are then replaced into random positions, and the simulation cell relaxed using conjugate gradients. We chose LAMMPS and the MNB potential [37] for the relaxations. During the relaxation, the x- and y- axes were constrained to zero strain, but the z- axis was allowed to relax to zero stress. These elastic boundary conditions are appropriate for simulating an irradiated thin surface layer, constrained by a semi-infinite substrate. This is appropriate for modelling self-ion irradiation in a thick sample [45]. The process of removing and replacing atoms builds up damage, with a canonical measure of the damage given by the ratio of the number of atoms repositioned to the number in the simulation. We displaced 1024 atoms per relaxation, corresponding to 6.25×10^{-4} cdpa per relaxation.

The MD simulations started with the CRA simulations at a range of cdpa values, given in table II. These were then strained in the x- and y- directions to the potential's lattice parameter at 300K. The simulation was then thermalized for 20 ps, with a Berendsen thermostat and barostat [46] to keep zero pressure in the z- direction. The MD simulations were performed using PARCAS [47–49] with the same potential used for the CRA simulations. Displacement cascades were initiated by shifting the cell randomly in x-, y- and z- directions, maintaining periodic boundary conditions, then giving the central atom 10 keV kinetic energy in a random direction. The cascade was followed with an electronic friction applied to atoms with kinetic energy over 10 eV [50] for 20 ps with a thermostat applied to the border atoms. Finally the simulation was followed for a further 10 ps with a barostat on the z-direction. A new cascade was then initiated. A canonical dpa level can be associated with these MD simulations by noting the number of vacancies produced per cascade initiated at the initial stages of damage production. From the first 40 cascades we estimate a cdpa level 4.1×10^{-6} per cascade.

An illustrative simulated microstructure at a dose 1.1 dpa is shown in figure 6. Note that vacancies are homogeneously dispersed, and dislocation loops of both interstitial and vacancy type can be seen. No isolated crowdions remain.

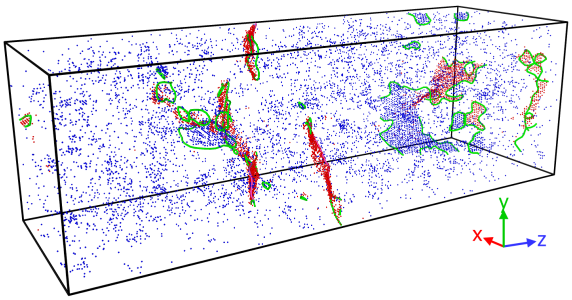

FIG. 6. Simulated microstructure at a dose 1.1 cdpa. Dislocation lines with Burgers vectors $1/2\langle 111\rangle$ (green) and $\langle 100\rangle$ (pink) generated using DXA[51]. Interstitials (red) and vacancies (blue) generated from Wigner-Seitz cell occupation [40]. Rendered using Ovito [52].

CRA dose (cdpa)	MD dose (cdpa)	total dose (cdpa)
0	0	0
0	4.1×10^{-5}	4.1×10^{-5}
0	1.63×10^{-4}	1.63×10^{-4}
0	4.07×10^{-4}	4.07×10^{-4}
0	0.00163	0.00163
0	0.00407	0.00407
0	0.00814	0.00814
0	0.0122	0.0122
0.00625	0.00651	0.0128
0.0188	0.00651	0.0253
0.0350	0.00651	0.0416
0.0625	0.00651	0.0691
0.113	0.00651	0.119
0.188	0.00651	0.194
0.350	0.00651	0.357
0.625	0.00651	0.633
1.13	0.00651	1.13
3.00	0.00651	3.01

TABLE II. Simulation parameters for generating high dose microstructures.

Experimental measurement

Samples of high purity tungsten (99.97 wt% purity, procured from Plansee) were annealed at 1500C for 24h in vacuum to allow full recrystallization, and then mechanically and electropolished using 0.1% NaOH solution to produce a mirror finish. Ion implantations were then performed at the Helsinki Accelerator Laboratory with 20 MeV W^{5+} ions [53]. A summary of the ion fluxes is given in table III together with a damage level computed using SRIM (Quick K-P method, assuming threshold displacement energy 68 eV.) These calculations also suggest the peak damage is at a depth 1.25 μm, falling to near zero at 2 μm. The peak concentration of injected ions is at 1.7 μm. A full description of the preparation and ion irradiation for these samples is given in ref [16]. We note that this set of samples has been analysed for other properties, including lattice strain [45] and hardness[54].

Incident Fluence (ions/cm^2)	Flux (ions/cm^2/s)	Damage level (SRIM) dpa
2.7 $\times 10^{10}$	6.24$\times 10^{8}$	1.0 $\times$ 10^{-4}
8.13$\times 10^{10}$	”	3.2 $\times$ 10^{-4}
2.42$\times 10^{11}$	3.1-5.0$\times 10^{8}$	0.0010
8.03$\times 10^{11}$	”	0.0032
2.55$\times 10^{12}$	”	0.010
4.61$\times 10^{12}$	”	0.018
8.20$\times 10^{12}$	”	0.032
1.42$\times 10^{13}$	”	0.056
2.54$\times 10^{13}$	”	0.10
8.11$\times 10^{13}$	”	0.32
2.53$\times 10^{14}$	”	1.0
8.10$\times 10^{14}$	1.12$\times 10^{11}$	3.2
2.53$\times 10^{15}$	”	10.0
8.10$\times 10^{15}$	”	32

TABLE III. Fluence and flux of the ion beam used to irradiate the samples. A damage level is computed using SRIM. Note that the flux is increased in steps to acheive higher fluences in a reasonable experimental time.

Thermal diffusivity measurements were made using laser-induced transient grating spectroscopy (TGS) [33, 55, 56]. This technique uses crossed, pulsed laser beams (0.5 ns duration, $\lambda = 532$ nm wavelength, 1 kHz repeat frequency) to generate a temperature grating at the sample surface. The time-dependent decay of this temperature grating is monitored by diffraction of two continuous wave probe beams that are detected using a fast photodiode connected to an oscilloscope. A detailed description of the experimental setup is provided elsewhere [57]. The thermal diffusivity is then determined from the decay of the diffracted intensity. A full description of the TGS set up for these measurements can be found in ref [16]. Calculations suggest the thermal diffusivity measured is dominated by a surface thickness $\sim \lambda/\pi$ [55], which in this case is 1 μm and so the measurement reported here is due to the thermal diffusivity changes in the implanted layer.

RESULTS

In figure 7 we show the athermal atom count for the relaxed, high-dose microstructure simulations as a histogram binned by potential energy. We can clearly see peaks at $\sim$ 0.3 eV corresponding to vacancies, and over 0.5 eV for interstitials. The total athermal atom count for these simulations is plotted in figure 8. Note that this is a count of all the atoms which have high energy, and not a count of point defects. The interstitial and total vacancy count in this figure were computed using a Wigner-Seitz analysis of the occupation of lattice sites, and the vacancy total separated into vacancy clusters and vacancy loops using the method of ref [40]. We see a saturation of athermal atoms above 0.1 cdpa at about 8% of the total atom count, while the vacancy concentration saturates at 0.3%. This illustrates how a defect in this model is treated as a spatially-diffuse scattering region, and not as the individual point defects.

In figure 9 we show the computed thermal diffusivity for the relaxed high dose microstructure simulations. On this plot we include the computed thermal diffusivity for CRA only simulations, with on MD cascade relaxation. We see that the unrelaxed CRA-only simulations show the correct general trend seen in the experiment, namely that the thermal diffusivity is significantly reduced at high dose but saturates over 0.1 dpa. But it is clear that the effect is overestimated. This is an expected consequence of the overestimation of the number of defects generated by the CRA method alone.

Also on figure 9 we show an estimate for the thermal diffusivity made by Reza et al. [16] due to TEM visible dislocation loops ($>$ 1.5 nm diameter). This model uses the area observed in loops in TEM images[58] to find a number of interstitial point defects. It is then assumed that each interstitial is paired with a vacancy, and the scattering rate per Frenkel pair is used to turn the observed point defect count into a maximum thermal diffusivity. As each interstitial is treated as a strong scattering source, even though it may be in the centre of a large dislocation loop and so locally appear as (strained) perfect crystal, this model must overestimate the scattering due to observed defects. However, this estimate clearly still underestimates the drop in diffusivity, indicating that visible damage is only a small contributor to the true change in thermal conductivity. In ref [16], the authors find a better absolute change in diffusivity by assuming defects too small to see follow a power-law distribution [50, 59], though can not track the shape of the curve well.

By contrast to these two estimates, the relaxed CRA+MD cascade simulations show a rate of thermal diffusivity reduction which is a good match to the experiment at doses $<$ 0.1 dpa, and the saturation level of a 50% reduction in thermal diffusivity for doses $>$ 0.1 dpa is also a match. This suggests the level of damage in the relaxed CRA+MD simulations is a good match to experiment at low fluence end where the defect clusters are small, through dislocation network formation at 0.01-0.1 dpa and through to the saturation dose of larger dislocation loop defects seen in figure 6 above 1 dpa.

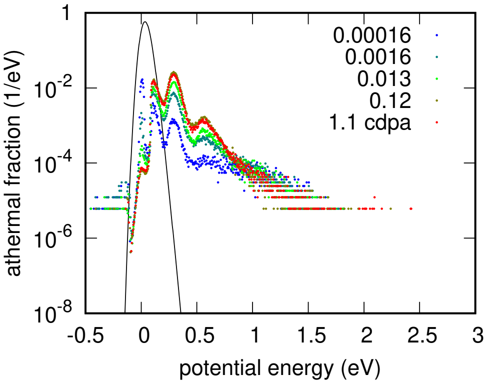

FIG. 7. A histogram of potential energies of high dose simulated microstructures. The solid line shows the expected fraction of atoms in each bin, normalised so that the area under the curve equals one. The symbols show the predicted fraction of non-thermal atoms (equation 9, for a range of doses.

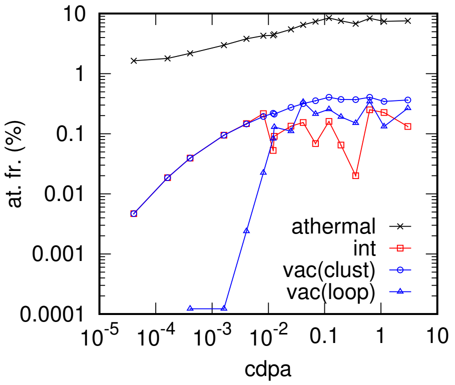

FIG. 8. Computed atomic fraction of athermal atoms and defect types for high dose CRA+MD simulations.

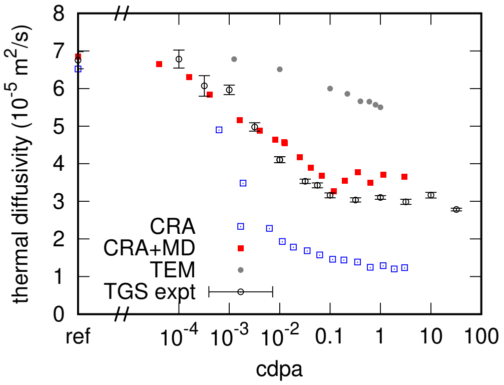

FIG. 9. Computed thermal diffusivity of MD simulated microstructures at a range of doses. Also shown experimentally measured diffusivity using Transient Grating Spectroscopy (TGS), and an estimate by Reza et al [16] of thermal diffusivity due to TEM-visible dislocation loops.

CONCLUSION

In this paper we have used a simple and empirical model for the scattering rate due to a defected atom - stating that the rate should be proportional to the local excess energy difference alone. This local energy is easy to compute and unambiguous in an MD simulation of a single component system, though we acknowledge that it is not simply accessible to a density functional theory calculation. However, after this first assumption, we have made no further approximations or experiment-specific parameterizations. We developed a simple analytic form for the expected distribution of potential energies, and from this used a statistical method to find the expected number of athermal atoms. This model can easily be used to post-analyse the output of any single component molecular dynamics simulations.

As electronic thermal transport properties are not accessible to classical empirical potentials, we needed to parameterize the absolute level of the thermal conductivity using established known single crystal experimental data, and we parameterized the scattering rate for the Frenkel pair defect using the established electrical resistivity data. At high dose the microstructure is one of network dislocations and dislocation loops with a homogeneous background of mono vacancies and small vacancy clusters, and the simulated thermal diffusivity we report is derived from all the athermal atoms.

An obvious extension to this model is to include substitutional impurity atoms as point sources of scattering. This was considered in ref [33], with rhenium atoms in tungsten taken as point sources of impurity scattering. As this approach showed an excellent agreement with experiment, we suggest it should be possible to include impurity atoms in the dilute limit in the present model in a similar way.

We conclude that our simple model is able to discriminate in a robust manner between undamaged (but strained) crystal, which has only a small contribution to conductivity loss, and highly distorted local environments near dislocation cores and vacancy cages where the scattering should be high. As it is fitted to the average scattering rate for a range of atomic environments near Frenkel pairs, correlates with weakly and strongly scattering regions, and correctly deduces the volume fraction of such atomic environments, it is a therefore a good estimator of the average change in thermal diffusivity in highly irradiated simulated microstructures.

ACKNOWLEDGEMENTS

This work has been carried out within the framework of the EUROfusion Consortium and has received funding from the Euratom research and training programme 2014-2018 and 2019-2020 under grant agreement No 633053 and from the RCUK [grant number EP/T012250/1]. To obtain further information on the data and models underlying this paper please contact PublicationsManager@ukaea.uk. The views and opinions expressed herein do not necessarily reflect those of the European Commission. We would like to thank Max Boleininger for stimulating discussions. Computer time granted by the IT Center for Science – CSC – Finland is gratefully acknowledged.

---

* Daniel.Mason@ukaea.uk
† mohamed.reza@eng.ox.ac.uk

[1] J. H. You, E. Visca, C. Bachmann, T. Barrett, F. Crescenzi, M. Fursdon, H. Greuner, D. Guilhem, P. Languille, M. Li, S. McIntosh, A. V. Müller, J. Reiser, M. Richou, and M. Rieth, "European DEMO divertor target: Operational requirements and material-design interface," vol. 9, pp. 171–176, 2016.

[2] A. J. H. Donné and W. Morris, *European Research Roadmap to the Realisation of Fusion Energy.* 11 2018.

[3] T. Hirai, S. Panayotis, V. Barabash, C. Amzallag, F. Escourbiac, A. Durocher, M. Merola, J. Linke, T. Loewenhoff, G. Pintsuk, M. Wirtz, and I. Uytdenhouwen, "Use of tungsten material for the ITER divertor," *Nuclear Materials and Energy*, vol. 9, pp. 616–622, 2016.

[4] M. Rieth, J. Boutard, S. Dudarev, T. Ahlgren, S. Antusch, N. Baluc, M.-F. Barthe, C. Becquart, L. Ciupinski, J. Correia, C. Domain, J. Fikar, E. Fortuna, C.-C. Fu, E. Gaganidze, T. Galán, C. García-Rosales, B. Gludovatz, H. Greuner, K. Heinola, N. Holstein, N. Juslin, F. Koch, W. Krauss, K. Kurzydlowski, J. Linke, C. Linsmeier, N. Luzginova, H. Maier, M. Martínez, J. Missiaen, M. Muhammed, A. Muñoz, M. Muzyk, K. Nordlund, D. Nguyen-Manh, P. Norajitra, J. Opschoor, G. Pintsuk, R. Pippan, G. Ritz, L. Romaner, D. Rupp, R. Schäublin, J. Schlosser, I. Uytdenhouwen, J. van der Laan, L. Veleva, L. Ventelon, S. Wahlberg, F. Willaime, S. Wurster, and M. Yar, "Review on the efda programme on tungsten materials technology and science," *Journal of Nuclear Materials*, vol. 417, no. 1, pp. 463–467, 2011. Proceedings of ICFRM-14.

[5] M. Fukuda, K. Yabuuchi, S. Nogami, A. Hasegawa, and T. Tanaka, "Microstructural development of tungsten and tungsten–rhenium alloys due to neutron irradiation in hfir," *Journal of Nuclear Materials*, vol. 455, no. 1, pp. 460–463, 2014. Proceedings of the 16th International Conference on Fusion Reactor Materials (ICFRM-16).

[6] A. Hasegawa, T. Tanno, S. Nogami, and M. Satou, "Property change mechanism in tungsten under neutron irradiation in various reactors," *Journal of Nuclear Materials*, vol. 417, no. 1, pp. 491–494, 2011. Proceedings of ICFRM-14.

[7] F. S. Khan and P. B. Allen, "Deformation potentials and electron-phonon scattering: Two new theorems," *Phys. Rev. B*, vol. 29, pp. 3341–3349, Mar 1984.

[8] A. Ganose, J. Park, A. Faghaninia, R. Woods-Robinson, K. Persson, and A. Jain, "Efficient calculation of carrier scattering rates from first principles," *Nature Comm.*, vol. 12, p. 2222, 2021.

[9] G. Madsen and D. Singh, "Boltztrap. a code for calculating band-structure dependent quantities," *Comp. Phys. Comm.*, vol. 175, pp. 67–71, 2006.

[10] L. C. R. Alfred, "Theory of the resistivity change in a metal due to multiple point imperfections," *Phys. Rev.*, vol. 152, pp. 693–698, Dec 1966.

[11] R. P. Gupta and R. Benedek, "Impurity scattering and residual resistivity of transition metals," *Phys. Rev. B*, vol. 19, pp. 583–586, Jan 1979.

[12] R. P. Gupta, "Residual resistivity of defects in metals," *Phys. Rev. B*, vol. 35, pp. 5431–5436, Apr 1987.

[13] C. Domain and C. Becquart, "Solute – ¡111¿ interstitial loop interaction in a-fe: A dft study," *Journal of Nuclear Materials*, vol. 499, pp. 582–594, 2018.

[14] P. M. Derlet and S. L. Dudarev, "Microscopic structure of a heavily irradiated material," *Phys. Rev. Materials*, vol. 4, p. 023605, Feb 2020.

[15] S. J. Zinkle, "Electrical resistivity of small dislocation loops in irradiated copper," *Journal of Physics F: Metal Physics*, vol. 18, pp. 377–391, mar 1988.

[16] A. Reza, H. Yu, K. Mizohata, and F. Hofmann, "Thermal diffusivity degradation and point defect density in self-ion implanted tungsten," *Acta Materialia*, vol. 193, pp. 270–279, 2020.

[17] C. Liu, L. He, Y. Zhai, B. Tyburska-Püschel, P. Voyles, K. Sridharan, D. Morgan, and I. Szlufarska, "Evolution of small defect clusters in ion-irradiated 3C-SiC: Combined cluster dynamics modeling and experimental study," *Acta Materialia*, vol. 125, pp. 377 – 389, 2017.

[18] D. R. Mason, X. Yi, A. E. Sand, and S. L. Dudarev, "Experimental observation of the number of visible defects produced in individual primary damage cascades in irradiated tungsten," *EPL (Europhysics Letters)*, vol. 122, no. 6, p. 66001, 2018.

[19] M. J. Caturla, T. Diaz de la Rubia, M. Victoria, R. Corzine, M. James, and G. Greene, "Multiscale modeling of radiation damage: applications to damage production by gev proton irradiation of cu and w, and pulsed irradiation effects in cu and fe," *Journal of Nuclear Materials*, vol. 296, no. 1, pp. 90–100, 2001. 4th Int. Workshop on Spallation Materials Technology.

[20] G. J. Ackland and A. P. Jones, "Applications of local crystal structure measures in experiment and simulation," *Phys. Rev. B*, vol. 73, p. 054104, Feb 2006.

[21] U. Bhardwaj, A. E. Sand, and M. Warrier, "Classification of clusters in collision cascades," *Computational Materials Science*, vol. 172, p. 109364, 2020.

[22] A. M. Goryaeva, C. Lapointe, C. Dai, J. Dérès, J.-B. Maillet, and M.-C. Marinica, "Reinforcing materials modelling by encoding the structures of defects in crystalline solids into distortion scores," *Nature Communications*, vol. 11, p. 4691, 2020.

[23] N. Mott and H. Jones, *The theory of the properties of metals and alloys.* Oxford University Press, Oxford, UK, 1936.

[24] D. Mason, "Incorporating non-adiabatic effects in embedded atom potentials for radiation damage cascade simulations," *Journal of Physics: Condensed Matter*, vol. 27, p. 145401, mar 2015.

[25] W. Baber, "The contribution to the electrical resistance of metals from collisions between electrons," *Proc. R. Soc. Lond.*, vol. A158, p. 383–396, 1936.

[26] Y. Y. Tsiovkin, A. N. Voloshinskii, V. V. Gapontsev, and V. V. Ustinov, "Residual electrical resistivity in dilute

nonmagnetic alloys of transition metals," *Phys. Rev. B*, vol. 71, p. 184206, May 2005.

[27] K. D. Rasch, R. W. Siegel, and H. Schultz, "Quenching and recovery investigations of vacancies in tungsten," *Philosophical Magazine A: Physics of Condensed Matter, Structure, Defects and Mechanical Properties*, vol. 41, no. 1, pp. 91–117, 1980.

[28] H. Shukovshy, R. Rose, and J. Wulff, "The low temperature electrical resistivity of lattice defects in deformed tungsten single crystals," *Acta Met.*, vol. 14, pp. 821–830, 1966.

[29] C. Broeders and A. Konobeyev, "Defect production efficiency in metals under neutron irradiation," *Journal of Nuclear Materials*, vol. 328, no. 2, pp. 197–214, 2004.

[30] H. e. Ullmaier, *Atomic defects in metals.* Berlin Heidelberg, 1991.

[31] S. Dudarev and A. Sutton, "Elastic interactions between nano-scale defects in irradiated materials," *Acta Materialia*, vol. 125, pp. 425 – 430, 2017.

[32] P.-W. Ma and S. L. Dudarev, "Universality of point defect structure in body-centered cubic metals," *Phys. Rev. Materials*, vol. 3, p. 013605, Jan 2019.

[33] F. Hofmann, D. Mason, J. Eliason, A. Maznev, K. Nelson, and S. Dudarev, "Non-contact measurement of thermal diffusivity in ion-implanted nuclear materials," *Scientific Reports*, vol. 15, p. 16042, 2015.

[34] S. Lovesey, *Theory of Neutron Scattering from Condensed Matter*, vol. 1. Oxford University Press, Oxford, UK., 1984.

[35] L.-M. Peng, G. Ren, S. Dudarev, and M. Whelan, "Debye-waller factors and absorptive scattering factors of elemental crystals," *Acta Crys*, vol. A52, pp. 456–470, 1996.

[36] S. Plimpton, "Fast parallel algorithms for short-range molecular dynamics," *Journal of Computational Physics*, vol. 117, no. 1, pp. 1 – 19, 1995.

[37] D. R. Mason, D. Nguyen-Manh, and C. S. Becquart, "An empirical potential for simulating vacancy clusters in tungsten," *Journal of Physics: Condensed Matter*, vol. 29, p. 505501, nov 2017.

[38] C. Ho, R. Powell, and P. Liley, "Thermal conductivity of the elements," *J. Phys. Chem. Ref. Data*, vol. 1, p. 279–421, 1972.

[39] M. W. Finnis and J. E. Sinclair, "A simple empirical n-body potential for transition metals," *Philosophical Magazine A*, vol. 50, no. 1, pp. 45–55, 1984.

[40] D. Mason, F. Granberg, M. Boleininger, T. Scharz-Selinger, K. Nordlund, and S. Dudarev, "Parameter-free quantitative simulation of high dose microstructure and hydrogen retention in ion-irradiated tungsten," 2021.

[41] F. Granberg, K. Nordlund, M. W. Ullah, K. Jin, C. Lu, H. Bei, L. M. Wang, F. Djurabekova, W. J. Weber, and Y. Zhang, "Mechanism of radiation damage reduction in equiatomic multicomponent single phase alloys," *Phys. Rev. Lett.*, vol. 116, no. 13, p. 135504, 2016.

[42] J. Byggmästar, F. Granberg, and K. Nordlund, "Effects of the short-range repulsive potential on cascade damage in iron," *J. Nucl. Mater.*, vol. 508, pp. 530–539, 2018.

[43] G. Velişa, M. W. Ullah, H. Xue, K. Jin, M. L. Crespillo, H. Bei, W. J. Weber, and Y. Zhang, "Irradiation-induced damage evolution in concentrated ni-based alloys," *Acta Mater.*, vol. 135, pp. 54–60, 2017.

[44] F. Granberg, J. Byggmästar, and K. Nordlund, "Defect accumulation and evolution during prolonged irradiation of Fe and FeCr alloys," *J. Nucl. Mater.*, vol. 528, p. 151843, 2020.

[45] D. R. Mason, S. Das, P. M. Derlet, S. L. Dudarev, A. J. London, H. Yu, N. W. Phillips, D. Yang, K. Mizohata, R. Xu, and F. Hofmann, "Observation of transient and asymptotic driven structural states of tungsten exposed to radiation," *Phys. Rev. Lett.*, vol. 125, p. 225503, Nov 2020.

[46] H. J. C. Berendsen, J. P. M. Postma, W. F. van Gunsteren, A. DiNola, and J. R. Haak, "Molecular dynamics with coupling to external bath," *J. Chem. Phys.*, vol. 81, no. 8, p. 3684, 1984.

[47] M. Ghaly, K. Nordlund, and R. S. Averback, "Molecular dynamics investigations of surface damage produced by kiloelectronvolt self-bombardment of solids," *Phil. Mag. A*, vol. 79, no. 4, pp. 795–820, 1999.

[48] K. Nordlund, M. Ghaly, R. S. Averback, M. Caturla, T. Diaz de la Rubia, and J. Tarus, "Defect production in collision cascades in elemental semiconductors and FCC metals," *Phys. Rev. B*, vol. 57, no. 13, pp. 7556–7570, 1998.

[49] K. Nordlund, "Molecular dynamics simulation of ion ranges in the 1 100 kev energy range," *Computational Materials Science*, vol. 3, no. 4, pp. 448 – 456, 1995.

[50] A. E. Sand, S. L. Dudarev, and K. Nordlund, "High-energy collision cascades in tungsten: Dislocation loops structure and clustering scaling laws," *EPL (Europhysics Letters)*, vol. 103, no. 4, p. 46003, 2013.

[51] A. Stukowski, V. V. Bulatov, and A. Arsenlis, "Automated identification and indexing of dislocations in crystal interfaces," *Modelling and Simulation in Materials Science and Engineering*, vol. 20, p. 085007, oct 2012.

[52] A. Stukowski, "Visualization and analysis of atomistic simulation data with OVITO–the open visualization tool," *Modelling and Simulation in Materials Science and Engineering*, vol. 18, p. 015012, dec 2009.

[53] P. Tikkanen, V. Palonen, H. Jungner, and J. Keinonen, "Ams facility at the university of helsinki," *Nucl. Instruments Methods Phys. Res. Sect. B Beam Interact. with Mater. Atoms.*, vol. 223-224, pp. 35–39, 2004.

[54] S. Das, "Recent advances in characterising irradiation damage in tungsten for fusion power," *SN Appl. Sci.*, vol. 1, p. 1614, 2019.

[55] O. Kading, H. Skurk, A. Maznev, and E. Matthias, "Transient thermal gratings at surfaces for thermal characterization of bulk materials and thin-films," *Appl. Phys. a*, vol. 61, pp. 253–261, 1995.

[56] F. Hofmann, M. Short, and C. Dennett, "Transient grating spectroscopy: An ultrarapid, nondestructive materials evaluation technique.," *MRS Bulletin*, vol. 44, p. 392–402, 2019.

[57] A. Reza, C. A. Dennett, M. P. Short, J. Waite, Y. Zayachuk, C. M. Magazzeni, S. Hills, and F. Hofmann, "Non-contact, non-destructive mapping of thermal diffusivity and surface acoustic wave speed using transient grating spectroscopy," *Review of Scientific Instruments*, vol. 91, no. 5, p. 054902, 2020.

[58] X. Yi, M. L. Jenkins, M. A. Kirk, Z. Zhou, and S. G. Roberts, "In-situ tem studies of 150 kev w+ ion irradiated w and w-alloys: Damage production and microstructural evolution," *Acta Materialia*, vol. 112, pp. 105–120, 2016.

[59] X. Yi, A. E. Sand, D. R. Mason, M. A. Kirk, S. G. Roberts, K. Nordlund, and S. L. Dudarev, "Direct ob-

servation of size scaling and elastic interaction between nano-scale defects in collision cascades," *EPL (Europhysics Letters)*, vol. 110, no. 3, p. 36001, 2015.